ACES Asian Chemical Editorial Society

doi.org/10.1002/asia.202400130

CHEMISTRY AN ASIAN JOURNAL Research Article

www.chemasianj.org

Zinc Doping Induces Enhanced Thermoelectric Performance of Solvothermal SnTe

Lijun Wang,[a] Xiao-Lei Shi,*[c] Lvzhou Li,[d] Min Hong,[e] Bencai Lin,[a] Pengcheng Miao,[a] Jianning Ding,[d] Ningyi Yuan,[a] Shuqi Zheng,*[b] and Zhi-Gang Chen*[c]

The creation of hierarchical nanostructures can effectively strengthen phonon scattering to reduce lattice thermal conductivity for improving thermoelectric properties in inorganic solids. Here, we use Zn doping to induce a remarkable reduction in the lattice thermal conductivity in SnTe, approaching the theoretical minimum limit. Microstructure analysis reveals that ZnTe nanoprecipitates can embed within SnTe grains beyond the solubility limit of Zn in the Zn alloyed SnTe. These nanoprecipitates result in a substantial decrease of the lattice thermal conductivity in SnTe, leading to an ultralow lattice thermal conductivity of 0.50 $W m^{-1} K^{-1}$ at 773 K and a peak ZT of ~0.48 at 773 K, marking an approximately 45% enhancement compared to pristine SnTe. This study underscores the effectiveness of incorporating ZnTe nanoprecipitates in boosting the thermoelectric performance of SnTe-based materials.

Introduction

Thermoelectric conversion technology, facilitating the direct conversion of heat into electricity, holds immense potential for applications in waste heat utilization, deep space exploration, silent refrigeration, wearable devices, and chip cooling.[1–10] The efficiency of thermoelectric devices (TEDs) is contingent upon the performance of thermoelectric materials, gauged through the figure-of-merit $ZT = S^2\sigma/\kappa$, where σ denotes electrical conductivity, S is the Seebeck coefficient, T represents absolute temperature, and κ is the total thermal conductivity. The κ encompasses the electrical contribution (κ_e) and lattice thermal conductivity (κ_l). Given the interconnected nature of these parameters, achieving optimal control over electrical and thermal performance has been a longstanding focus in thermoelectrics.[11,12]

Over the last three decades, thermoelectric research has witnessed substantial achievements, marked by the continual emergence of new materials and a more profound comprehension of electron and phonon transport mechanisms. PbTe-based material, positioned as the top performer in the mid-temperature thermoelectric range, has attained a ZT value well beyond 2.[13,14] Nevertheless, the toxicity associated with lead (Pb) has posed a barrier to the wide practical application of PbTe. Consequently, recent research efforts have been directed towards the development of high-performance lead-free alternatives to PbTe. Among them, cost-effective SnTe has garnered attention due to its analogous valence band structure and crystal structure to PbTe, establishing it as the most promising candidate material for replacing PbTe.

However, in comparison to PbTe, pristine SnTe demonstrates inferior thermoelectric performance. The primary disparity arises from the energy offset (ΔE) (0.35 eV) between the light-hole band at the L point and the heavy-hole band at the Σ point in SnTe, which is significantly larger than that in PbTe (0.17 eV). The substantial ΔE in SnTe implies a minimal contribution of the heavy-hole band to the S, leading to a relatively low S for SnTe.[15–17] Moreover, owing to the lower atomic mass of Sn compared to Pb, the κ_l of SnTe (3.5 $W m^{-1} K^{-1}$ at 300 K) surpasses that of PbTe (1.5 $W m^{-1} K^{-1}$ at 300 K).[18,19] In essence, the amalgamation of low electrical performance and high κ culminates in an inherently inferior ZT value for pristine SnTe (0.4) when juxtaposed with PbTe.[20] To overcome these challenges in SnTe, researchers have devoted significant efforts to enhance its ZT value by optimizing electron and phonon transport processes. Effective strategies involve improving the electrical performance of SnTe by band engineering, such as optimizing carrier concentration n,[21–23] manipulating band convergence,[24–27] introducing resonant states,[19,28] and inducing

[a] L. Wang, B. Lin, P. Miao, N. Yuan
School of Material Science & Engineering, National Experimental Demonstration Center for Materials Science and Engineering, Jiangsu Province Cultivation base for State Key Laboratory of Photovoltaic Science and Technology, Changzhou University, Changzhou, Jiangsu, 213164, China

[b] S. Zheng
State Key Laboratory of Heavy Oil Processing, College of New Energy and Materials, China University of Petroleum, Beijing, 102249, China
E-mail: zhengsq09@163.com

[c] X.-L. Shi, Z.-G. Chen
School of Chemistry and Physics, ARC Research Hub in Zero-emission Power Generation for Carbon Neutrality, and Centre for Materials Science, Queensland University of Technology, Brisbane, Queensland 4000, Australia
E-mail: xiaolei.shi@qut.edu.au
zhigang.chen@qut.edu.au

[d] L. Li, J. Ding
Yangzhou Technology Innovation Research Center for Carbon Neutrality of Yangzhou University, School of Mechanical Engineering, Yangzhou University, Yangzhou 225127, Jiangsu, China

[e] M. Hong
Centre for Future Materials and School of Engineering, University of Southern Queensland, Springfield Central, Queensland 4300, Australia

Supporting information for this article is available on the WWW under https://doi.org/10.1002/asia.202400130

energy filtering.[29,30] Also, approaches aimed at diminishing the thermal conduction of SnTe involve phonon engineering, such as nanostructuring,[31,32] hierarchical architectures,[33–35] defects modulation,[36] and incorporation of dense dislocations and precipitates.[37] All these strategies collectively contribute to enhancing the *ZT* value, and the optimized SnTe has obtained a competitive maximum *ZT* of 1.4~1.8 at 900 K,[38–40] nearly comparable to PbTe.

Recent studies indicate that incorporating alloying phases into the SnTe matrix generates various defects, such as point defects, dislocation, and precipitates, which serve as potent phonon scattering centers. This proves to be an effective strategy for reducing thermal conduction. These phases include Cu_2Q (Q=Se, Te),[41,42] SrTe,[17] Bi_2O_3,[29] $AgMTe_2$ (M=Sb, Bi),[43,44] MgAgSb.[45] For instance, various defects can be induced into the SnTe matrix by alloying SnTe with $CuSbSe_2$, including Cu-based nanoprecipitates, dislocations, and point defects, leading to an ultra-low κ_l of 0.40 $W m^{-1} K^{-1}$.[46] Cd and Cu_2Te Co-doping SnTe can induce an "eutectoid" precipitation, including CdTe and Cu_2Te-based nano-phases, leading to an ultra-low κ_l of 0.42 $W m^{-1} K^{-1}$.[37] By introducing Bi_2O_3 into the SnTe matrix, the nanoprecipitates significantly reduce the κ_l, leading to an enhanced average power factor ($S^2\sigma$).[29] Hence, combining SnTe with a well-designed secondary phase proves to be an effective approach to enhancing thermoelectric performance.

In this study, we employ an efficient microwave-synthesized approach to introduce ZnTe nanoprecipitates into the SnTe matrix, as illustrated in Figure 1a. The detailed process was described in the supporting information. Microstructural characterization reveals the presence of nanoprecipitates and nanopores induced into the SnTe matrix by Zn doping. With a high density of nanoprecipitates, nanopores, and grain boundaries, phonons are significantly scattered with different wavelengths (Figure 1b), leading to a low κ_l of 0.50 $W m^{-1} K^{-1}$ at 773 K, approaching the amorphous limit of κ_l. Concurrently, Zn-doping effectively facilitates valence band convergence, compensating for the reduced *S* and ensuring the final improvement in $S^2\sigma$. Consequently, the *ZT* values of all doped samples are higher than those of the pure SnTe sample (~0.33 at 773 K), as depicted in Figure 1c. The maximum *ZT* values of ~0.47 and ~0.48 are achieved for $Sn_{0.98}Zn_{0.02}Te$ and $Sn_{0.97}Zn_{0.03}Te$ specimens at 773 K, respectively, representing an improvement of ~45% compared to pure SnTe. This enhancement is attributed to Zn doping, which does not compromise the inherent $S^2\sigma$ of SnTe but significantly reduces the κ_l. Moreover, ZnTe nanoprecipitates, attached to grain boundaries and/or embedded in the matrix, contribute to the reduction of κ_l.

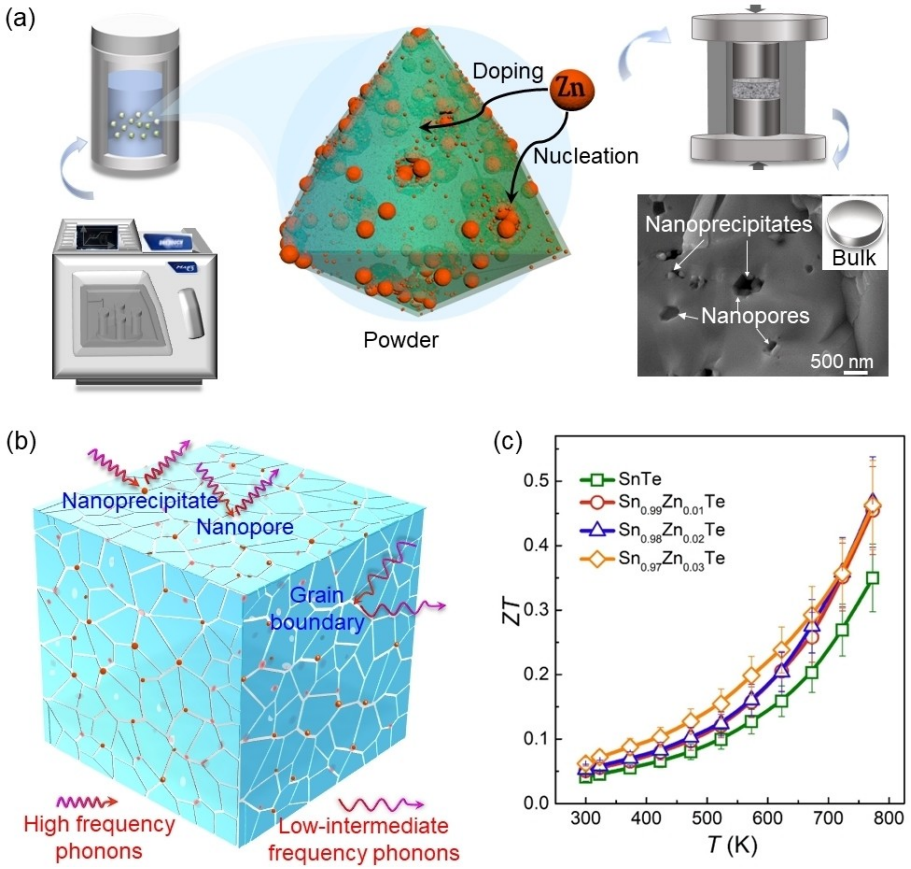

Figure 1. Schematic illustrations of the preparation of thermoelectric materials containing nanoprecipitates and schematic diagram of phonon scattering mechanisms. (**a**) The microwave method combined spark plasma sintering technology for the preparation of Zn-doped SnTe thermoelectric materials. (**b**) Schematic diagram of the mechanism of enhanced phonon scattering by nanoprecipitates, nanopores, and grain boundaries. (**c**) Temperature-dependent *ZT* values for as-sintered $Sn_{1-x}Zn_xTe$.

Results and Discussion

The XRD data for the SnTe powder synthesized *via* a microwave method were refined using GSAS, and the results are presented in Figure 2a. Figure 2b shows the Rietveld refined crystallographic information file (CIF) diagram of the SnTe sample, revealing a cubic rock-salt structure (space group $Fm\bar{3}m$) with lattice parameters $a=b=c=6.328$ Å and angles $\alpha=\beta=\gamma=90°$. Figure 2c displays the XRD patterns of the as-synthesized $Sn_{1-x}Zn_xTe$ ($x=0$, 0.01, 0.02, and 0.03) powders. All diffraction peaks for the samples match the rock-salt structure of SnTe (space group $Fm\bar{3}m$, PDF#46-1210), and no impurity phases are observed. To assess the impact of Zn-doping on the phase structure of SnTe, we analyzed the variation of the (200) diffraction peak and lattice parameter with the doping amount, as shown in Figures 2d–e. Notably, with increasing Zn-doping, a slight right shift of the (200) peak is observed. This should be attributed to the fact that the doped Zn replaces the Sn site while the ironic radius of Zn^{2+} (0.74 Å) is smaller than that of Sn^{2+} (0.93 Å).[47,48] As shown in Figure 2e, the lattice parameter monotonously decreases with the increase of Zn content, consistent with the reduction of ionic radius from Sn^{2+} to Zn^{2+}.

Figure 3 presents SEM micrographs of the as-synthesized $Sn_{1-x}Zn_xTe$ ($x=0$, 0.01, 0.02, 0.03). All $Sn_{1-x}Zn_xTe$ grains display a regular octahedral structure, indicating that microwave stimulation promotes the preferential growth of $Sn_{1-x}Zn_xTe$ along the $<111>$ crystal direction.[33,49] The pure SnTe grains have uniform sizes with smooth surfaces (Figure 3a). However, in Zn-doped SnTe samples, small nanoprecipitates are embedded in the SnTe matrix (Figure 3b), particularly noticeable in $Sn_{0.98}Zn_{0.02}Te$ (Figures 3c–d). With an increase in Zn doping, more nanoprecipitates are observed; in $Sn_{0.97}Zn_{0.03}Te$ grains, some nanoprecipitates are embedded in the SnTe matrix, while others are attached to the surface, as shown in Figure 3e. Interestingly, the $Sn_{0.97}Zn_{0.03}Te$ exhibits a misshapen octahedral morphology. The observed shape change, as seen in other nanostructures with an FCC structure,[49,50] suggests that Zn dopants can induce a surface energy change in SnTe. EDS mapping analysis was performed on $Sn_{0.97}Zn_{0.03}Te$ to determine the elemental distribution of the nanoprecipitates. The results revealed that the chemical composition of the nanoprecipitate phase is rich in Zn, while the matrix is deficient in Sn, as illustrated in Figures 3f–h. It suggests that the nanoprecipitate should be ZnTe. However, no ZnTe impurity can be detected in the powder XRD results (Figure 2c), possibly due to the low amount of ZnTe. Figure S1 presents a TEM image of a $Sn_{0.97}Zn_{0.03}Te$ with a size of approximately 5 μm, appearing to be surrounded by nanoprecipitates. The corresponding EDS element mapping indicates that Sn and Te are uniform distribution in the sample, while the nanoprecipitates are rich in

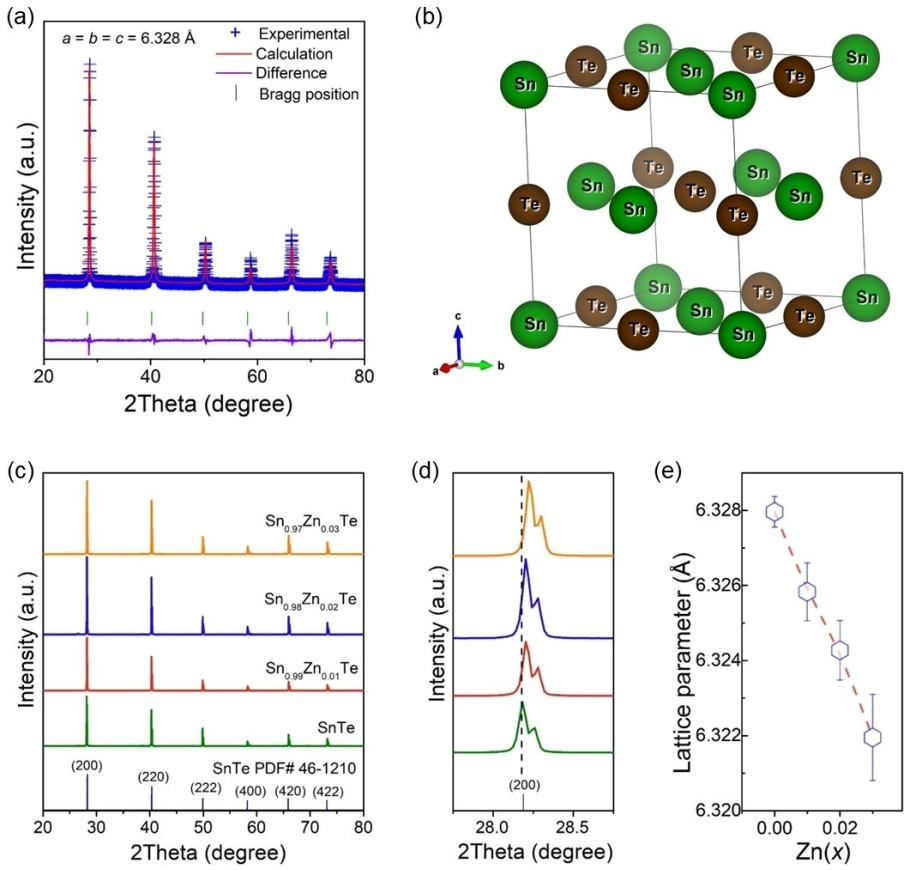

Figure 2. Crystal Characteristics of the as-synthesized $Sn_{1-x}Zn_xTe$ ($x=0$, 0.01, 0.02, and 0.03). (**a**) XRD Rietveld refinement of the as-synthesized SnTe powder. (**b**) Crystal structure simulation for the cubic SnTe. (**c**) Powder XRD patterns of the as-synthesized $Sn_{1-x}Zn_xTe$ ($x=0$, 0.01, 0.02, 0.03). (**d**) Enlarged view of (200) diffraction peak. (**e**) Lattice parameter as a function of Zn content.

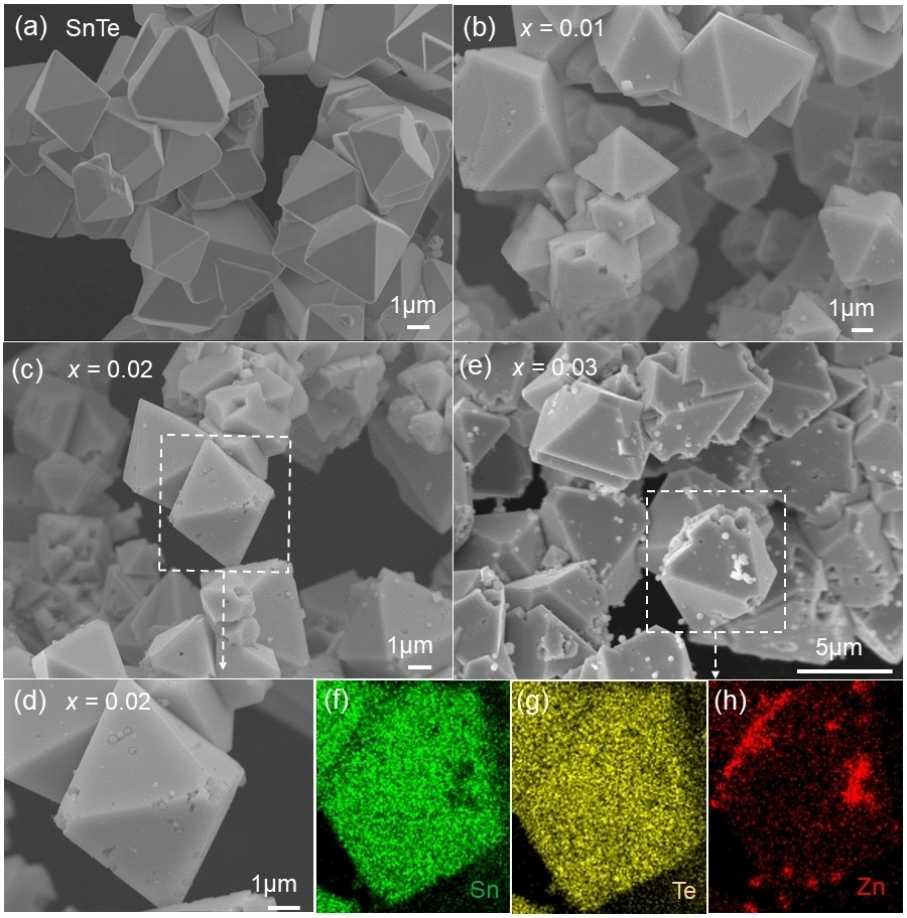

Figure 3. Microstructure characteristics of the as-synthesized $Sn_{1-x}Zn_xTe$ ($x=0$, 0.01, 0.02, and 0.03). SEM images of synthesized (**a**) SnTe, (**b**) $Sn_{0.99}Zn_{0.01}Te$, (**c–d**) $Sn_{0.98}Zn_{0.02}Te$, (**e**) $Sn_{0.97}Zn_{0.03}Te$. (**f–h**) corresponding EDS mapping of $Sn_{0.97}Zn_{0.03}Te$ grain selected in **e**.

Zn. The corresponding EDS line scan results confirm the enrichment of Zn. We attribute the inhomogeneities within the matrix to the reduction of κ_l, contributing to the improved thermoelectric performance.

To investigate the effect of Zn doping on the as-sintered $Sn_{1-x}Zn_xTe$ ($x=0$, 0.01, 0.02, 0.03) pellet after SPS, their crystal structures were analyzed by XRD, and the results are depicted in Figure 4a. All the samples are mainly composed of cubic SnTe (PDF#46-1210) at room temperature. When $x=0.02$, a small amount of ZnTe (PDF#15-0746) can be detected, indicating that the solid solubility of Zn in SnTe is less than 2%.[47] With further increasing Zn content, amounts of ZnTe phases are observed in the XRD pattern of the as-sintered $Sn_{1-x}Zn_xTe$ ($x=$ 0, 0.01, 0.02, 0.03). However, no second phase of ZnTe was observed in the XRD patterns of the as-synthesized $Sn_{1-x}Zn_xTe$ (Figure 2c). Small amounts of nanoparticles were found in the SEM images of the powder sample (Figure 3), which could be ascribed to the crystal growth of the ZnTe second phase during sintering, resulting in the observation of the ZnTe second phase in the bulk samples. As can be seen from the amplified (200) diffraction peak, the (200) diffraction peak of the as-sintered $Sn_{1-x}Zn_xTe$ slightly shifts to the right, mainly due to the ionic radius of Zn^{2+} (0.74 Å) being smaller than that of Sn^{2+} (0.93 Å),[48] which is consistent with the XRD results of the as-synthesized $Sn_{1-x}Zn_xTe$ ($x=0$, 0.01, 0.02, 0.03).

Figure 4b shows the cross-sectional morphology of the as-sintered $Sn_{1-x}Zn_xTe$ ($x=0$, 0.01, 0.02, 0.03) pellet. As can be observed, the grains resulting from the SPS processing with an average size of 5.0 μm remain intact. Some grain boundaries are easily visible. For pure SnTe, a small number of cracks at the grain boundary reduce its density. The densities of all the pellets were measured and the results are shown in Table 1. Figures 4c–d show the cross-sectional morphology of the as-sintered $Sn_{0.97}Zn_{0.03}Te$. A great number of nanopores can be seen at the grain boundaries and in the matrix of $Sn_{0.97}Zn_{0.03}Te$, resulting in a decrease in the density of the as-sintered

Table 1. Densities of the as-sintered $Sn_{1-x}Zn_xTe$ ($x=0$, 0.01, 0.02, 0.03) pellet. The theoretical density of SnTe is 6.46 g cm^{-3}.

Compositions	Densities (d, g cm^{-3})	Relative density
SnTe	6.25	96.7%
$Sn_{0.99}Zn_{0.01}Te$	6.19	95.8%
$Sn_{0.98}Zn_{0.02}Te$	6.12	94.7%
$Sn_{0.97}Zn_{0.03}Te$	6.10	94.4%

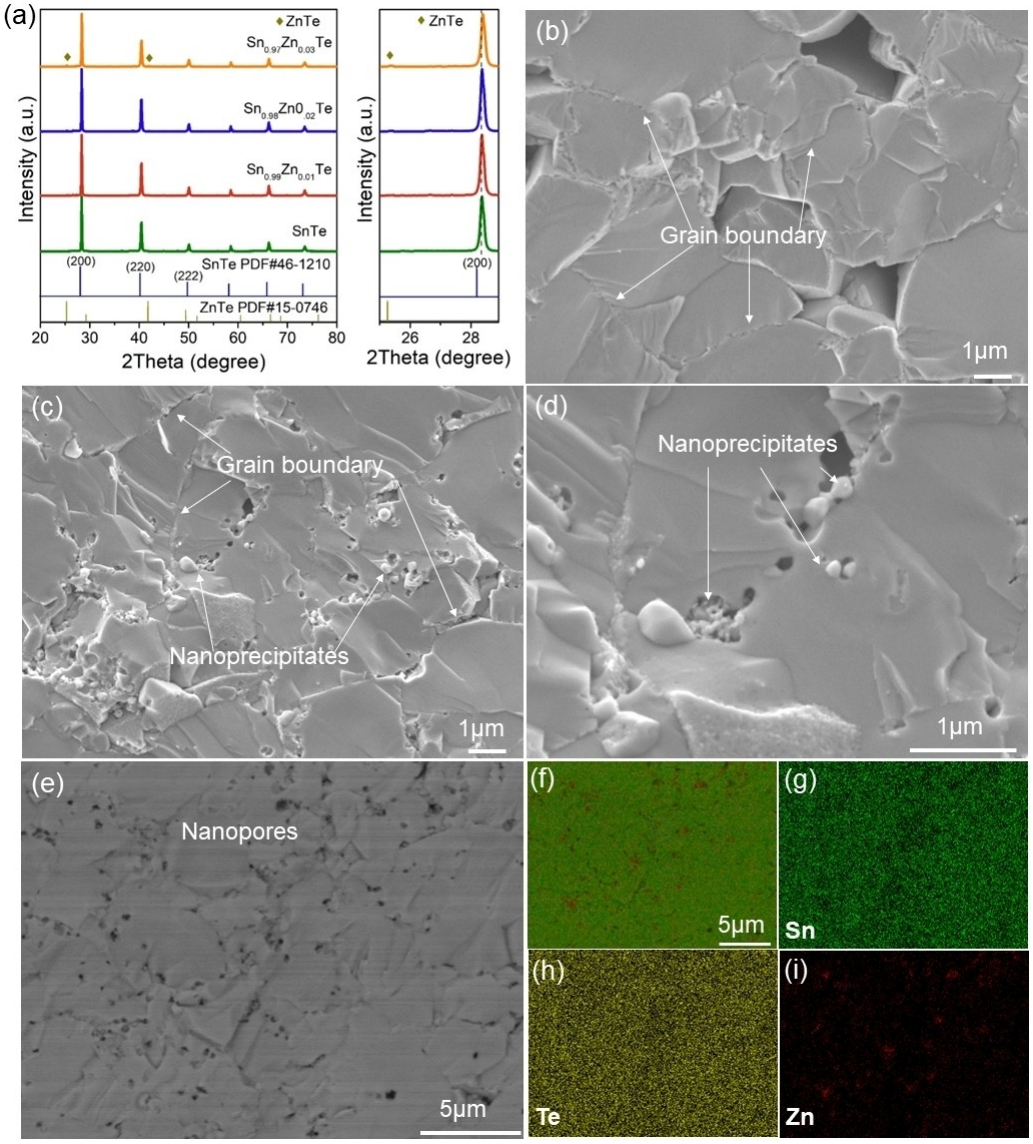

Figure 4. Crystal and microstructure characteristics of the as-sintered $Sn_{1-x}Zn_xTe$ ($x = 0$, 0.01, 0.02, and 0.03). (**a**) XRD patterns of the as-sintered $Sn_{1-x}Zn_xTe$ ($x = 0$, 0.01, 0.02, 0.03) pellets, and enlarged view of (200) diffraction peak. (**b**) SEM images of SnTe, showing grain boundary. (**c**) SEM images of $Sn_{0.97}Zn_{0.03}Te$, showing grain boundary and nanoprecipitates. (**d**) Enlarged SEM images of the $Sn_{0.97}Zn_{0.03}Te$, clearly showing nanoprecipitates. (**e**) BSE image of the as-sintered $Sn_{0.97}Zn_{0.03}Te$ and (**f–i**) corresponding EDS mapping of Sn, Te, and Zn.

$Sn_{0.97}Zn_{0.03}Te$ (Table 1). Interestingly, most nanoprecipitates are embedded in the nanopores, while small amounts of nanoparticles are attached to the surface, as shown in Figure 4c. To verify the presence of the nanoprecipitates and nanopores, a backscattered electron (BSE) image (Figure 4e) was taken for the as-sintered $Sn_{0.97}Zn_{0.03}Te$. Nanopores are visible at the grain boundaries and in the as-sintered $Sn_{0.97}Zn_{0.03}Te$ matrix. From the corresponding EDS maps (Figures 4f–i), Te homogeneously distributes in the as-sintered $Sn_{0.97}Zn_{0.03}Te$ matrix while Sn is absent in the Zn-rich areas. The EDS mapping supports the formation of the ZnTe impurity, which has been verified by XRD (Figure 4a). It is interesting to note that all the Zn-rich areas exit the nanopores. The BSE image further confirms the conjecture, that is, ZnTe nanoprecipitates distribute at the grain boundaries and/or embed in the interior of the SnTe grains. The formation of ZnTe nanoprecipitates can play an important role in reducing the κ_l through additional phonon scattering, and this relationship will be further discussed.

Figure 5 plots the temperature-dependent thermoelectric performance of the as-sintered $Sn_{1-x}Zn_xTe$ ($x = 0$, 0.01, 0.02, 0.03) pellets. Consistent with the typical behavior of degenerate semiconductors, the σ of all samples decreases as temperature increases (Figure 5a). Moreover, nearly all doped samples exhibit a slightly lower σ compared to the pristine sample. The decrease in σ is more pronounced with higher Zn concentration, attributed to the introduction of impurities/defects and reduced carrier mobility caused by increased carrier scattering.[51] The temperature-dependent S of the as-sintered $Sn_{1-x}Zn_xTe$ ($x = 0$, 0.01, 0.02, 0.03) is illustrated in Figure 5b. The positive S values indicate p-type conductivity. Furthermore, the

S increases with both temperature and Zn doping until $x = 0.02$. Zn substitution-induced reduction in Sn vacancies may lead to a decrease in the hole concentration. However, when $x = 0.03$, the excessive formation of Zn-driven precipitates increases the electron concentration, leading to a slight decrease in the *S* for $Sn_{0.97}Zn_{0.03}Te$.[47] The $S^2\sigma$ of both the pure and doped samples are illustrated in Figure 5c. For pure SnTe, the $S^2\sigma$ ranges from 11.0 to 17.9 $\mu W cm^{-1} K^{-2}$ across the temperature range of 300–773 K. Due to the increased *S*, the $S^2\sigma$ of the as-sintered $Sn_{1-x}Zn_xTe$ ($x = 0.01$ and 0.02) are enhanced, with the $x = 0.02$ sample reaching the maximum value of 19.5 $\mu W cm^{-1} K^{-2}$ at 773 K. This value is comparable to those observed for In-doped SnTe[28] and Ag&In co-doped SnTe.[52]

Figure 5d illustrates the temperature-dependent κ of the as-sintered $Sn_{1-x}Zn_xTe$ ($x = 0$, 0.01, 0.02, 0.03) pellets. A significant reduction in κ is evident for the as-sintered $Sn_{1-x}Zn_xTe$ compared to pristine SnTe. Furthermore, the κ demonstrates a decreasing trend with increasing Zn doping, attributed to both diminished electronic (κ_e) and lattice (κ_l) contributions. The κ of pristine SnTe ranges from ~8.14 to 3.97 $W m^{-1} K^{-1}$ from 300 to 773 K, dramatically decreasing to ~5.05 to 2.75 $W m^{-1} K^{-1}$ after doping with a 3% fraction of Zn. The κ_e was calculated

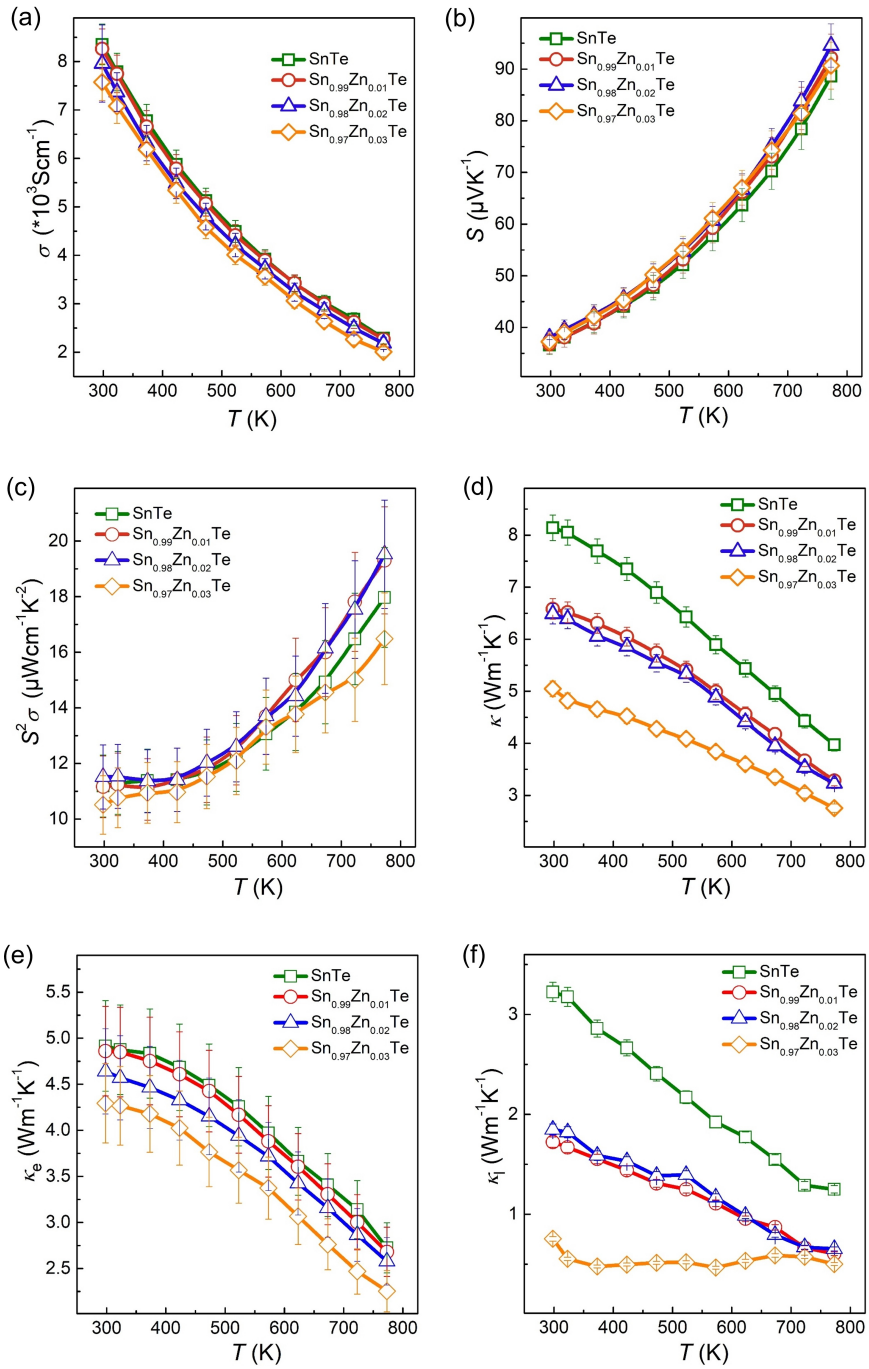

Figure 5. Temperature-dependent (**a**) σ; (**b**) *S*; (**c**) $S^2\sigma$; (**d**) κ; (**e**) κ_e, and (**f**) κ_l of the sintered $Sn_{1-x}Zn_xTe$ ($x = 0$, 0.01, 0.02, 0.03) pellets.

according to the Wiedemann-Franz law $\kappa_e = L\sigma T$, where L is the Lorenz number and can be empirically determined by $L = 1.5 + \exp[\frac{|S|}{116}]$, where L is in $10^{-8}\,W\Omega K^{-2}$, and S in $\mu V K^{-1}$.[53] As depicted in Figure 5e, the temperature-dependent κ_e decreases with increasing Zn doping, a result of the decrease in temperature-dependent σ (Figure 5a). To clarify the underlying mechanism for the reduced κ, the κ_l was estimated by subtracting the κ_e from the κ. Figure 5f shows that the κ_l decreases with increasing temperature for both pristine and Zn-doped samples. The κ_l value for pristine SnTe ranges from 3.2 to 1.25 $W m^{-1} K^{-1}$ within the temperature range of 300 to 773 K. Remarkably, the κ_l of the as-sintered $Sn_{1-x}Zn_xTe$ exhibits a significant reduction with increasing Zn doping. Specifically, the κ_l for the as-sintered $Sn_{0.97}Zn_{0.03}Te$ decreases from 0.75 $W m^{-1} K^{-1}$ at 300 K to 0.50 $W m^{-1} K^{-1}$ at 773 K, approaching the amorphous limit of κ_l (0.4~0.5 $W m^{-1} K^{-1}$).[54] This should be due to the increase in impurity concentration after doping, leading to an increase in phonon scattering, especially the ZnTe nanoprecipitates on grain boundaries and in the SnTe matrix are more effective in scattering long wavelength phonons.[48] Furthermore, the introduction of point defects resulting from the slight substitution of Zn into the SnTe lattice induces the scattering of short-wavelength phonons, contributing to a further reduction in the κ_l.

We computed the electronic band structure and density of states (DOS) for $Sn_{27}Te_{27}$ and $Sn_{26}ZnTe_{27}$. The band structure of $Sn_{27}Te_{27}$ illustrates that the primary light-hole valence band (VB1) occurs at the L point and the secondary heavy-hole valence band (VB2) Σ point (Figure 6a). The band gap (E_g) of SnTe is direct with a value of 0.12 eV. A ΔE of 0.30 eV is observed between the two valence bands[33] Figure 6b presents the band structure of $Sn_{26}ZnTe_{27}$. It can be noted that the introduction of Zn leads to an E_g value of 0.28 eV and an ΔE value of 0.04 eV, revealing the convergence of two valence bands. The DOS of SnTe and Zn-doped SnTe are calculated and illustrated in Figures 6c–d. The introduction of Zn doping results in a significant distortion at the band gap edge, which is highlighted by a red line. This distortion is primarily attributed to Zn s-orbital. Consequently, the band convergence resulting from Zn doping contributes to the enhancement of the *S*. Although Zn doping in SnTe induces band convergence, the *S* does not increase significantly. This could be attributed to the low solid solubility of Zn in SnTe during our doping process, which may not have reached a level capable of effectively enhancing electrical performance.[47,48]

Conclusions

A facile approach has been developed to enhance the thermoelectric performance of SnTe by introducing ZnTe nanoprecipitates into the matrix. Crystal structure analysis reveals that the

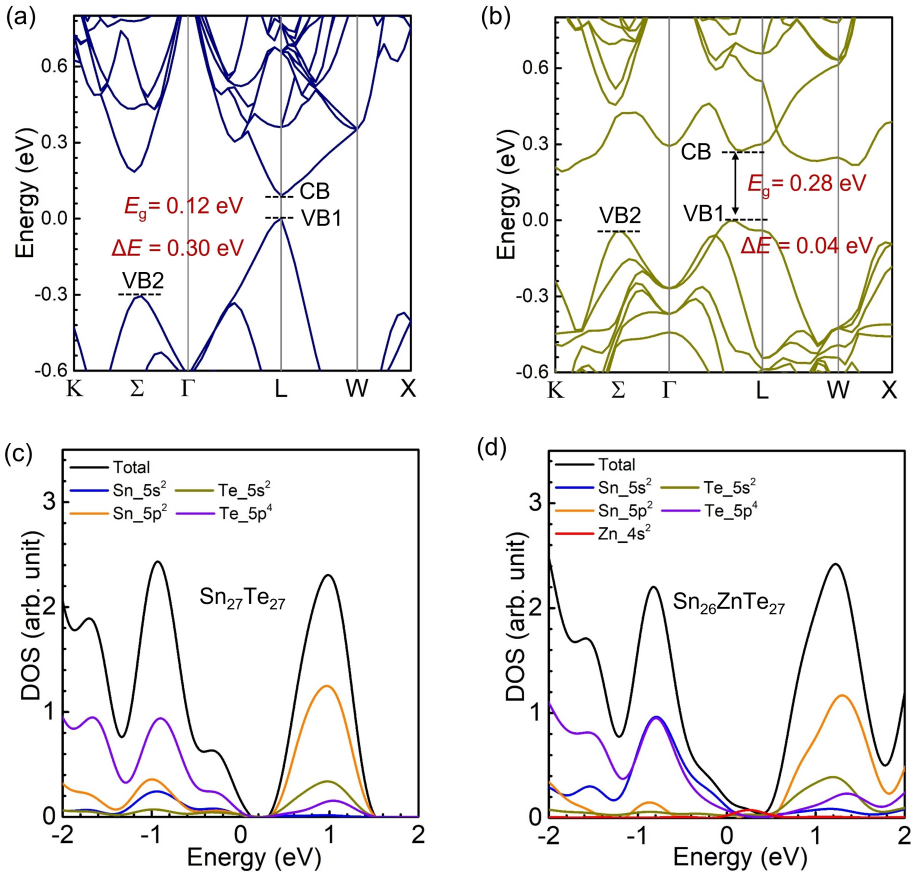

Figure 6. Calculated band structures for (**a**) $Sn_{27}Te_{27}$ and (**b**) $Sn_{26}ZnTe_{27}$. DOS near the Fermi level for (**c**) $Sn_{27}Te_{27}$ and (**d**) $Sn_{26}ZnTe_{27}$.

solid solubility of Zn in SnTe is less than 2%, and excessive Zn doping induces the formation of ZnTe nanoprecipitates, embedded in the SnTe matrix. The resultant increase in the S and decrease in the σ, caused by the ZnTe impurity phase, contribute to a slight improvement in the $S^2\sigma$ compared to pure SnTe. Importantly, the introduction of ZnTe impurities nanoprecipitates significantly reduces the κ by suppressing the κ_l. The low κ_l of 0.50 $W m^{-1} K^{-1}$ at 773 K for the as-sintered $Sn_{0.97}Zn_{0.03}Te$ is approximately 60% less than that of pure SnTe (1.25 $W m^{-1} K^{-1}$ at 773 K). The peak ZT of 0.48 for the as-sintered $Sn_{0.97}Zn_{0.03}Te$ at 773 K represents a 45% improvement over pure ZnTe. Potential further optimization of thermoelectric performance can be achieved by combining co-doping to improve the $S^2\sigma$ and introducing nanoprecipitation to reduce the κ_l.

Supporting Information

The detailed experimental process. TEM image of $Sn_{0.97}Zn_{0.03}Te$ and corresponding element distribution for $Sn_{0.97}Zn_{0.03}Te$. The corresponding EDS line scan results of $Sn_{0.97}Zn_{0.03}Te$. Above all are described in the supporting information.

Acknowledgements

This work is financially supported by the Special Fund for Science and Technology Innovation of Jiangsu Province (BE2022610). The authors would like to express their gratitude for the facilities, scientific, and technical assistance provided by the Australian Microscopy & Microanalysis Research Facility at the Centre for Microscopy and Microanalysis, The University of Queensland, and China University of Petroleum, Beijing. This work was enabled by the use of the Central Analytical Research Facility hosted by the Institute for Future Environments at QUT. Open Access publishing facilitated by Queensland University of Technology, as part of the Wiley - Queensland University of Technology agreement via the Council of Australian University Librarians.

Conflict of Interests

The authors declare no competing financial interest.

Data Availability Statement

The data that support the findings of this study are available from the corresponding author upon reasonable request.

Keywords: thermoelectric materials · SnTe · lattice thermal conductivity · ZnTe · nanoprecipitate

[1] Q. Yang, S. Yang, P. Qiu, L. Peng, T.-R. Wei, Z. Zhang, X. Shi, L. Chen, *Science* **2022**, *377*, 854–858.
[2] D. Liu, D. Wang, T. Hong, Z. Wang, Y. Wang, Y. Qin, L. Su, T. Yang, X. Gao, Z. Ge, B. Qin, L.-D. Zhao, *Science* **2023**, *380*, 841–846.
[3] B. Jiang, W. Wang, S. Liu, Y. Wang, C. Wang, Y. Chen, L. Xie, M. Huang, J. He, *Science* **2022**, *377*, 208–213.
[4] L. Xie, L. Yin, Y. Yu, G. Peng, S. Song, P. Ying, S. Cai, Y. Sun, W. Shi, H. Wu, N. Qu, F. Guo, W. Cai, H. Wu, Q. Zhang, K. Nielsch, Z. Ren, Z. Liu, J. Sui, *Science* **2023**, *382*, 921–928.
[5] S. Roychowdhury, T. Ghosh, R. Arora, M. Samanta, L. Xie, K. Singh Niraj, A. Soni, J. He, V. Waghmare Umesh, K. Biswas, *Science* **2021**, *371*, 722–727.
[6] J. Mao, G. Chen, Z. Ren, *Nat. Mater.* **2021**, *20*, 454–461.
[7] G. Hu, H. Edwards, M. Lee, *Nat. Electron.* **2019**, *2*, 300–306.
[8] Q. Zhang, K. Deng, L. Wilkens, H. Reith, K. Nielsch, *Nat. Electron.* **2022**, *5*, 333–347.
[9] Y. Jia, Q. Jiang, H. Sun, P. Liu, D. Hu, Y. Pei, W. Liu, X. Crispin, S. Fabiano, Y. Ma, Y. Cao, *Adv. Mater.* **2021**, *33*, 2102990.
[10] S. Yang, P. Qiu, L. Chen, X. Shi, *Small Science* **2021**, *1*, 2100005.
[11] G. J. Snyder, E. S. Toberer, *Nat. Mater.* **2008**, *7*, 105–114.
[12] H. Min, S. Shuai, L. Wanyu, L. Meng, L. Weidi, S. Xiao-Lei, C. Zhi-Gang, *Soft Sci.* **2023**, *3*, 29.
[13] K. Biswas, J. He, I. D. Blum, C. I. Wu, T. P. Hogan, D. N. Seidman, V. P. Dravid, M. G. Kanatzidis, *Nature* **2012**, *489*, 414–418.
[14] Z. Chen, Z. Jian, W. Li, Y. Chang, B. Ge, R. Hanus, J. Yang, Y. Chen, M. Huang, G. J. Snyder, *Adv. Mater.* **2017**, *29*, 1606768.
[15] Z. Chen, X. Guo, F. Zhang, Q. Shi, M. Tang, R. Ang, *J. Mater. Chem. A* **2020**, *8*, 16790–16813.
[16] L. M. Rogers, *J. Phys. D* **1968**, *1*, 845.
[17] L.-D. Zhao, X. Zhang, H. Wu, G. Tan, Y. Pei, Y. Xiao, C. Chang, D. Wu, H. Chi, L. Zheng, S. Gong, C. Uher, J. He, M. G. Kanatzidis, *J. Am. Chem. Soc.* **2016**, *138*, 2366–2373.
[18] Y. Pei, L. Zheng, W. Li, S. Lin, Z. Chen, Y. Wang, X. Xu, H. Yu, Y. Chen, B. Ge, *Adv. Electron. Mater.* **2016**, *2*, 1600019.
[19] G. Tan, W. G. Zeier, F. Shi, P. Wang, G. J. Snyder, V. P. Dravid, M. G. Kanatzidis, *Chem. Mater.* **2015**, *27*, 7801–7811.
[20] V. P. Vedeneev, S. P. Krivoruchko, E. P. Sabo, *Semiconductors* **1998**, *32*, 241–244.
[21] Z. Zhou, J. Yang, Q. Jiang, X. Lin, J. Xin, A. Basit, J. Hou, B. Sun, *Nano Energy* **2018**, *47*, 81–88.
[22] F. Guo, B. Cui, M. Guo, J. Wang, J. Cao, W. Cai, J. Sui, *Mater. Today Phys.* **2019**, *11*, 100156.
[23] M. Zhou, Z. M. Gibbs, H. Wang, Y. Han, C. Xin, L. Li, G. J. Snyder, *Phys. Chem. Chem. Phys.* **2014**, *16*, 20741–20748.
[24] H. Wu, C. Chang, D. Feng, Y. Xiao, X. Zhang, Y. Pei, L. Zheng, D. Wu, S. Gong, Y. Chen, J. He, M. G. Kanatzidis, L.-D. Zhao, *Energy Environ. Sci.* **2015**, *8*, 3298–3312.
[25] A. Banik, U. S. Shenoy, S. Anand, U. V. Waghmare, K. Biswas, *Chem. Mater.* **2015**, *27*, 581–587.
[26] R. Al Rahal Al Orabi, N. A. Mecholsky, J. Hwang, W. Kim, J.-S. Rhyee, D. Wee, M. Fornari, *Chem. Mater.* **2016**, *28*, 376–384.
[27] J. Tang, B. Gao, S. Lin, X. Wang, X. Zhang, F. Xiong, W. Li, Y. Chen, Y. Pei, *ACS Energy Lett.* **2018**, *3*, 1969–1974.
[28] G. Tan, F. Shi, S. Hao, H. Chi, L.-D. Zhao, C. Uher, C. Wolverton, V. P. Dravid, M. G. Kanatzidis, *J. Am. Chem. Soc.* **2015**, *137*, 5100–5112.
[29] T. Hong, C. Guo, D. Wang, B. Qin, C. Chang, X. Gao, L.-D. Zhao, *Mater. Today Energy* **2022**, *25*, 100985.
[30] Z. Ma, C. Wang, J. Lei, D. Zhang, Y. Chen, Y. Wang, J. Wang, Z. Cheng, *Nanoscale* **2020**, *12*, 1904–1911.
[31] L. Wang, S. Zheng, H. Chen, *J. Electron. Mater.* **2017**, *46*, 2847–2853.
[32] M. Hong, Y. Wang, S. Xu, X. Shi, L. Chen, J. Zou, Z.-G. Chen, *Nano Energy* **2019**, *60*, 1–7.
[33] L. Wang, M. Hong, Q. Sun, Y. Wang, L. Yue, S. Zheng, J. Zou, Z.-G. Chen, *ACS Appl. Mater. Interfaces* **2020**, *12*, 36370–36379.
[34] L. Wang, M. Hong, Y. Kawami, Q. Sun, V. T. Nguyen, Y. Wang, L. Yue, S. Zheng, Z. Zhu, J. Zou, Z.-G. Chen, *Sustain. Mater. Technol.* **2020**, *25*, e00183.
[35] Q. Jiang, H. Hu, J. Yang, J. Xin, S. Li, G. Viola, H. Yan, *ACS Appl. Mater. Interfaces* **2020**, *12*, 23102–23109.
[36] A. Abbas, M. Nisar, Z. H. Zheng, F. Li, B. Jabar, G. Liang, P. Fan, Y.-X. Chen, *ACS Appl. Mater. Interfaces* **2022**, *14*, 25802–25811.
[37] X. Qi, Y. Huang, D. Wu, B. Jiang, B. Zhu, X. Xu, J. Feng, B. Jia, Z. Shu, J. He, *J. Mater. Chem. A* **2020**, *8*, 2798–2808.
[38] R. Moshwan, W.-D. Liu, X.-L. Shi, Y.-P. Wang, J. Zou, Z.-G. Chen, *Nano Energy* **2019**, *65*, 104056.
[39] J. Hwang, H. Kim, M.-K. Han, J. Hong, J.-H. Shim, J.-Y. Tak, Y. S. Lim, Y. Jin, J. Kim, H. Park, *ACS Nano* **2019**, *13*, 8347–8355.

[40] R. Pathak, D. Sarkar, K. Biswas, *Angew. Chem. Int. Ed.* **2021**, *60*, 17686–17692.
[41] J. Tang, B. Gao, S. Lin, J. Li, Z. Chen, F. Xiong, W. Li, Y. Chen, Y. Pei, *Adv. Funct. Mater.* **2018**, *28*, 1803586.
[42] D. Li, H. W. Ming, J. M. Li, J. Zhang, X. Y. Qin, W. Xu, *ACS Appl. Energ. Mater.* **2019**, *2*, 8966–8973.
[43] T. Hong, D. Wang, B. Qin, X. Zhang, Y. Chen, X. Gao, L.-D. Zhao, *Mater. Today Phys.* **2021**, *21*, 100505.
[44] G. Tan, F. Shi, H. Sun, L.-D. Zhao, C. Uher, V. P. Dravid, M. G. Kanatzidis, *J. Mater. Chem. A* **2014**, *2*, 20849–20854.
[45] Z. Ma, C. Wang, J. Lei, D. Zhang, Y. Chen, J. Wang, Z. Cheng, Y. Wang, *ACS Appl. Energ. Mater.* **2019**, *2*, 7354–7363.
[46] H. Xu, H. Wan, R. Xu, Z. Hu, X. Liang, Z. Li, J. Song, *J. Mater. Chem. A* **2023**, *11*, 4310–4318.
[47] Z. Chen, R. Wang, G. Wang, X. Zhou, Z. Wang, C. Yin, Q. Hu, B. Zhou, J. Tang, R. Ang, *Chin. Phys. B* **2018**, *27*, 047202.
[48] M. Aminzare, Y.-C. Tseng, A. Ramakrishnan, K.-H. Chen, Y. Mozharivskyj, *Sustain. Energy Fuels* **2019**, *3*, 251–263.
[49] L. Wang, S. Chang, S. Zheng, T. Fang, W. Cui, P.-p. Bai, L. Yue, Z.-G. Chen, *ACS Appl. Mater. Interfaces* **2017**, *9*, 22612–22619.
[50] L. Yang, Z.-G. Chen, M. Hong, L. Wang, D. Kong, L. Huang, G. Han, Y. Zou, M. Dargusch, J. Zou, *Nano Energy* **2017**, *31*, 105–112.
[51] M. H. Lee, D.-G. Byeon, J.-S. Rhyee, B. Ryu, *J. Mater. Chem. A* **2017**, *5*, 2235–2242.
[52] L. J. Zhang, P. Qin, C. Han, J. L. Wang, Z. H. Ge, Q. Sun, Z. X. Cheng, Z. Li, S. X. Dou, *J. Mater. Chem. A* **2018**, *6*, 2507–2516.
[53] H.-S. Kim, Z. M. Gibbs, Y. Tang, H. Wang, G. J. Snyder, *APL Mater.* **2015**, *3*, 041506.
[54] D. G. Cahill, S. K. Watson, R. O. Pohl, *Phys. Rev. B* **1992**, *46*, 6131–6140.

Manuscript received: February 18, 2024
Accepted manuscript online: February 21, 2024
Version of record online: ■■, ■■

RESEARCH ARTICLE

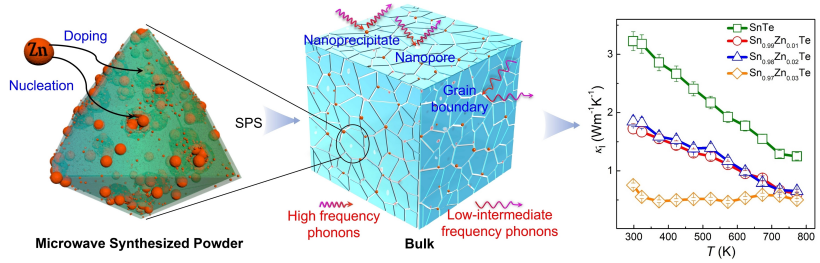

L. Wang, X.-L. Shi, L. Li, M. Hong, B. Lin, P. Miao, J. Ding, N. Yuan, S. Zheng*, Z.-G. Chen**

1 – 10

Zinc Doping Induces Enhanced Thermoelectric Performance of Solvothermal SnTe

We report a microwave-assisted wet chemical method for doping Zn into SnTe thermoelectric materials to *in-situ* induce rich ZnTe nanoprecipitates, nanopores, a large number of grain boundaries and other multi-dimensional defects. While ensuring competitive electrical transport performance, the introduced multi-dimensional defects induced phonon scattering across the entire scale, reducing the lattice thermal conductivity of SnTe to the amorphous limit and enhancing its thermoelectric performance.